



# MISTRAL and its KIDs

A. Paiella<sup>1,2</sup> · P. de Bernardis<sup>1,2</sup> · F. Cacciotti<sup>1</sup> · A. Coppolecchia<sup>1,2</sup> · S. Masi<sup>1,2</sup> · E. Barbavara<sup>1</sup> · E. S. Battistelli<sup>1,2,3</sup> · E. Carretti<sup>4</sup> · F. Columbro<sup>1,2</sup> · A. Cruciani<sup>2</sup> · G. D'Alessandro<sup>1,2</sup> · M. De Petris<sup>1,2</sup> · F. Govoni<sup>3</sup> · G. Isopi<sup>1</sup> · L. Lamagna<sup>1,2</sup> · P. Marongiu<sup>3</sup> · L. Mele<sup>1,2</sup> · E. Molinari<sup>3</sup> · M. Murgia<sup>3</sup> · A. Navarrini<sup>3</sup> · A. Orlati<sup>5</sup> · G. Pettinari<sup>6</sup> · F. Piacentini<sup>1,2</sup> · T. Pisanu<sup>3</sup> · S. Poppi<sup>3</sup> · G. Presta<sup>1,2</sup> · F. Radiconi<sup>1</sup>

Received: 31 October 2021 / Accepted: 13 August 2022  
© The Author(s) 2022

## Abstract

The Millimetric Sardinia radio Telescope Receiver based on Array of Lumped elements KIDs, MISTRAL, is a cryogenic W-band (77–103 GHz) LEKID camera which will be integrated at the Gregorian focus of the 64 m aperture Sardinia Radio Telescope, in Italy, in Autumn 2022. This instrument, thanks to its high angular resolution ( $\sim 13$  arcsec) and the wide instantaneous field of view ( $\sim 4$  arcmin), will allow continuum surveys of the mm-wave sky with a variety of scientific targets, spanning from extragalactic astrophysics to solar system science. In this contribution, we will describe the design of the MISTRAL camera, with a particular focus on the optimisation and test of a prototype of the focal plane.

**Keywords** LEKIDs · W-band · Ground-based telescope

## 1 Science Case

High angular resolution observations in the W-band allow to explore scientific targets which span from extragalactic astrophysics to solar system science. In the context of extragalactic astrophysics, through the Sunyaev-Zel'dovich effect [1], surveys of galaxy clusters can be obtained as well as information about their

---

✉ A. Paiella  
alessandro.paiella@roma1.infn.it

<sup>1</sup> Dipartimento di Fisica, Sapienza Università di Roma, P.le A. Moro 2, 00185 Rome, Italy

<sup>2</sup> INFN, Sezione di Roma, P.le A. Moro 2, 00185 Rome, Italy

<sup>3</sup> INAF, Osservatorio Astronomico di Cagliari, Via della Scienza 5, 09047 Selargius, CA, Italy

<sup>4</sup> INAF, Istituto di Radioastronomia, Via P. Gobetti 101, 40129 Bologna, Italy

<sup>5</sup> INAF, Istituto di Radioastronomia, Via Fiorentina 3513, 40059 Medicina, BO, Italy

<sup>6</sup> CNR, Istituto di Fotonica e Nanotecnologie, Via del Fosso del Cavaliere 100, 00133 Rome, Italy

physics, and the filaments connecting them [2]. The hot gas present in galaxy clusters can scatter, through the inverse Compton scattering, the photons of the cosmic microwave background (CMB) radiation leaving a very characteristic signature on the CMB spectrum: this is the Sunyaev-Zel'dovich effect (SZE). The SZE is a very powerful tool to observe galaxy clusters allowing to study them up to their low density parts and outskirts [3]. Since the SZE provides a measure of the integrated electron pressure along the line-of-sight, resolved measurements can identify intracluster medium discontinuities such as cold fronts or shocks, which are related to cluster mergers [4].

## 2 The MISTRAL Instrument

MISTRAL is a cryogenic camera consisting of a cryostat, provided by QMC Instruments [5], hosting a 4 K re-imaging optical system, composed of two Silicon lenses with anti-reflection coating in RO3003 [6] (provided by Cardiff University), and an about 400-pixel array of lumped element kinetic inductance detectors (LEKIDs), working in the W-band, between 77 and 103 GHz, cooled down to about 270 mK by a Chase Twin GL10 refrigerator [7], see Fig. 1 and Refs. [8–10].

MISTRAL will be installed at the Gregorian focus of the Sardinia Radio telescope (SRT) [11], the largest Italian radio telescope, located near Cagliari, in Sardinia, in Italy. SRT is a fully steerable radio telescope, with a 64 m diameter primary mirror and can host a maximum of 14 receivers, with a spectral coverage from 0.3 to 115 GHz [12]. For high angular resolution observations in the W-band, SRT+MISTRAL will be very competitive with the state-of-the-art of such an instrument: the Green Bank Telescope [13] with the TES-based MUSTANG2 instrument [14].

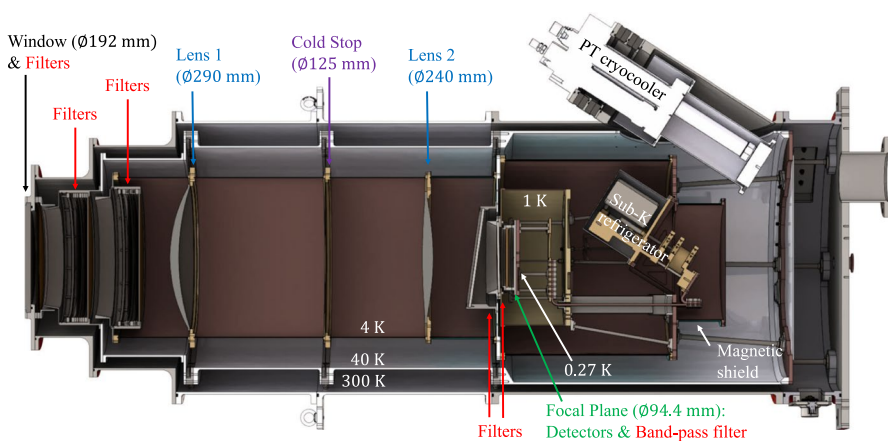


**Fig. 1** Rendering of the MISTRAL camera. The main parts such as the optical system, the pulse tube cryocooler, the sub-K refrigerator and the focal plane are indicated with arrows and different colors

### 3 The MISTRAL Detectors

As introduced before, LEKIDs are the detector technology chosen for the MISTRAL instrument. KIDs are low-temperature, fast, superconductive detectors, where radiation is detected if its energy ( $h\nu$ ) is greater than the binding energy of the Cooper Pairs of the superconductor ( $2\Delta \approx 3.5 k_B T_c$ , where  $T_c$  is the critical temperature of the superconducting film). In this way, the Cooper Pairs can be broken, and a change in the kinetic inductance is produced [15]. In the lumped element configuration, a superconducting strip is shaped and sized to perform as a radiation absorber as well as an inductor, which is coupled to a capacitor to form a high- $Q$  resonator [16].

Since the size of the aberration-corrected focal plane of MISTRAL is 94.4 mm diameter (which corresponds to an instantaneous field of view  $\sim 4$  arcmin), the detector array consists of about 400 pixels,  $\sim 3 \text{ mm} \times 3 \text{ mm}$  wide, spacing 4.2 mm on equilateral triangular cell, hosted on a 100 mm diameter Si wafer, see Fig. 2. In this way, the filling factor of the detector array and the angular resolution of MISTRAL are maximised.

#### 3.1 Simulations

The main parameters of the receiver system, such as the dielectric substrate thickness and the geometry of the absorber, have been chosen by optimising the absorption efficiency and spectrum through optical simulations [17–19]. The thickness and material of the dielectric substrate has been optimised in [20] with the aim to

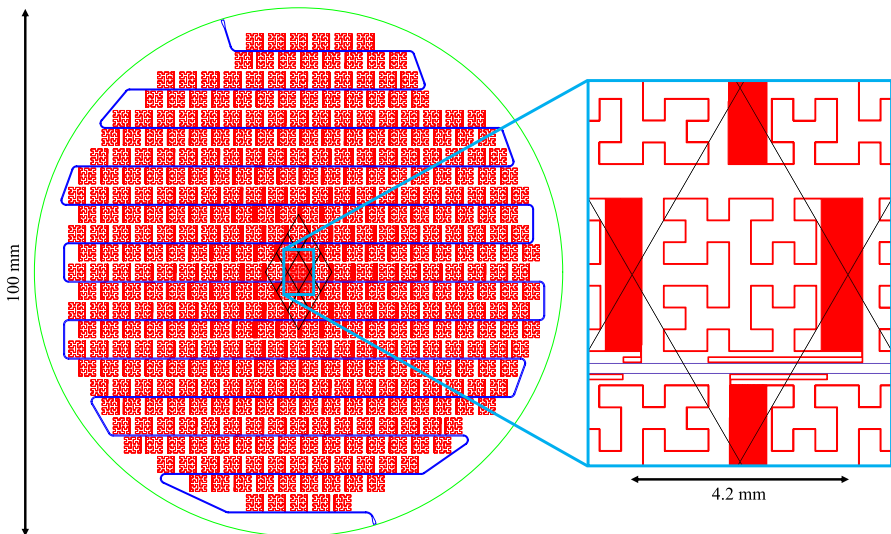


**Fig. 2** CAD drawing of the KID array: the feedline in blue, the KIDs in red and the green circumference represents the Si wafer (100 mm diameter). Some rhombus cells (4.2 mm side and smaller diagonal) are indicated in black and a zoom of the central cell is in the cyan box

have the absorption peak around 90 GHz and an absorption efficiency as constant as possible in the MISTRAL band (77–103 GHz): we obtained Silicon 235 mm thick. Here, we focus on the absorber geometry and size, assuming that the superconducting film is in Ti–Al bilayer 10 + 30 nm thick, with  $T_c \sim 945$  mK (see Sec. 3.2) and  $R_{\square} = 1 \Omega/\square$  [21]. Ti–Al bilayer films have superconducting gaps ( $\Delta$ ) which allow to build KIDs sensitive in the W-band ( $h\nu > 2\Delta$ ) [22–24]. The feedline for the KIDs will be a  $50\Omega$ -matched, Al 21 nm thick microstrip with a ground plane (realised in Al 200 nm thick) on the rear side of the Si substrate, which acts also as a radiation backshort. This feedline, with  $T_c \sim 1.4$  K, is not sensitive to W-band radiation.

Simulations have been carried out with HFSS [25], taking advantage of the periodicity of the detector array. The periodic cell is a rhombus with side and smaller diagonal 4.2 mm long, see Fig. 2. The HFSS design is shown in the *left panel* of Fig. 3. A Floquet port allows to define a periodic excitation, a plane wave in our case, while the *master/slave* boundary conditions on the lateral surface of the cell volume guarantee the periodicity [26]. The *right panel* of Fig. 3 shows the results of the absorption efficiency spectrum (absorbed power normalised to the plane wave input power with 2 polarisations) for different size of a 3rd order Hilbert geometry of the absorber [27] (the 90 deg rotation of the absorber inside the rhombus cell in the HFSS design with respect the actual CAD does not affect the results). The trade-off between in-band absorption efficiency and size for the detector packaging on the array leads to an optimal absorber design with  $h = 420$  mm and  $w = 4$  mm.

The Floquet port allows to simulate infinitely extended objects with a periodic geometry. Moreover, in our simulations, we consider only the KID inductor, which is the nominally absorbing part of the KIDs, thus neglecting the KID and coupling capacitors and the feedline needed for detector operation. Therefore, our results are more representative of pixels far from the edge of the wafer, where boundary effects might affect electromagnetic propagation and absorption, and in the limit where the total area of the rhomboid cell is dominated by the Hilbert-shaped absorber. The

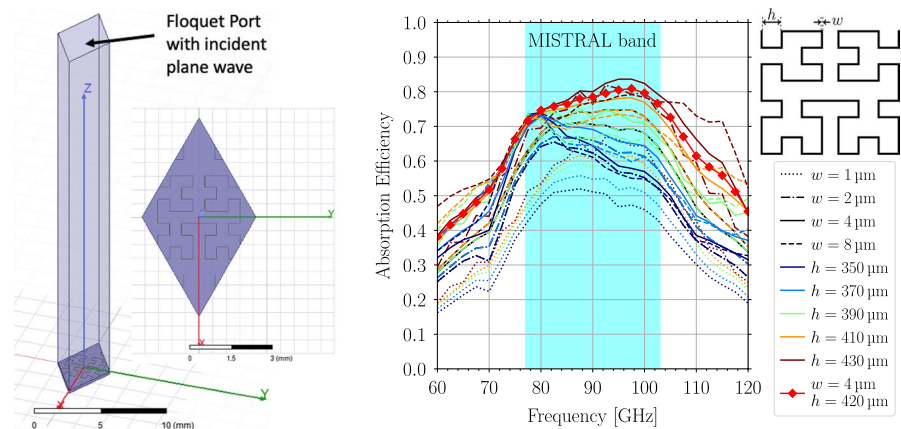


**Fig. 3** *Left panel*: Trimetric and top view of the HFSS design for the absorption simulation. *Right panel*: Absorption spectrum for different size of the 3rd order Hilbert absorber

total area of the cell in the final array is in fact occupied for the 60% by the inductor/absorber, for the 3% by the feedline, and depending on the pixel, from 16 to 2% by the KID and coupling capacitors, and from 21 to 35% is empty.

### 3.2 Prototype Array and Measurements

We designed a 31-pixel prototype array with resonant frequencies between 200 and 700 MHz, exploiting the entire 500 MHz bandwidth of our readout electronics [28, 29] and arranged in such a way to study different frequency spacing between near resonances. The resonators are designed to have the following values for quality factors at an operating temperature of 150 mK:  $Q_i > 50000$ ,  $Q_c \sim 20000$  and  $Q_{tot} \sim 15000$ . The prototype has been fabricated at CNR-IFN in Rome and is shown in Fig. 4, mounted inside its aluminum holder.

In dark conditions, we measured the scattering  $S_{21}$  parameter in order to check that the quality factors were as expected, and how many pixels were alive: we found 30 over 31 working detectors, see the *left panel* of Fig. 5, and we measured the expected values for the quality factors. Moving from 150 mK to the operating temperature of MISTRAL of 270 mK, we measured a reduction of the  $Q_i$  of a factor 3, a reduction of  $Q_{tot}$  of a factor 1.5 and a reduction of the dynamics of a factor 2. We also measured the critical temperature of the Ti–Al bilayer 10 + 30 nm thick:  $T_c \sim 945$  mK, see the *right panel* of Fig. 5. According to the BCS theory, this  $T_c$  corresponds to a cut-on frequency of about 70 GHz which falls indeed below the MISTRAL frequency band.

Moreover, we studied the behaviour of the resonators under a static magnetic field. The magnetic field has been produced thanks to a coil realised outside the cryostat in such a way the detector holder was at the center of this coil, see the *left panel* of Fig. 6. The magnetic field was produced during the cooling down before the aluminum detector holder and the detector array became superconducting in

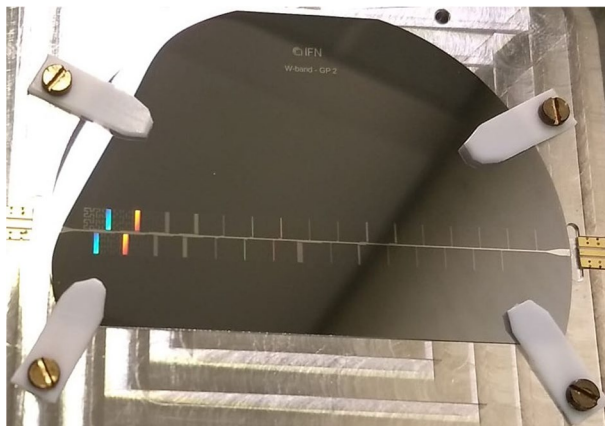


**Fig. 4** Picture of the 31-pixel prototype, mounted inside its Al holder by means of 4 Teflon clamps

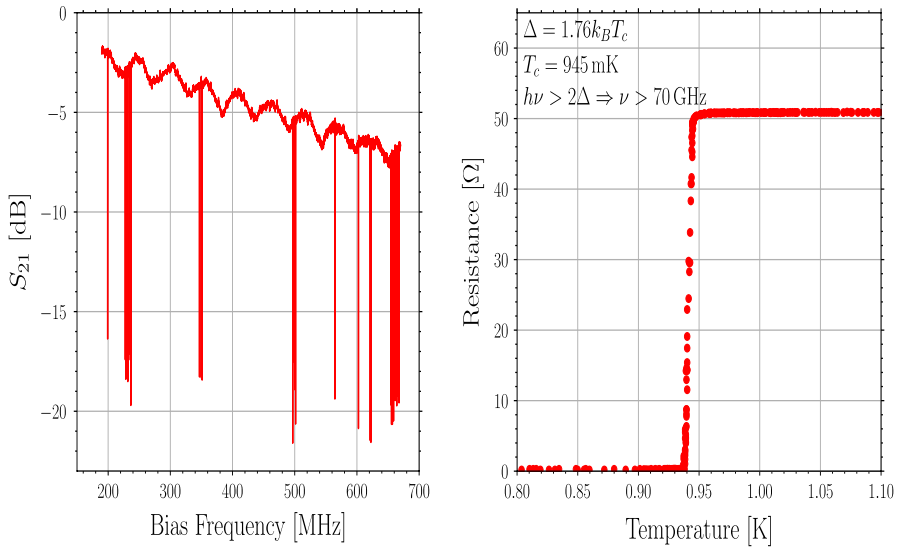


**Fig. 5** *Left panel:* Amplitude of the  $S_{21}$  parameter measured, for the 31-pixel prototype, in dark conditions and at an operating temperature of 150 mK. *Right panel:* Measurement of the critical temperature of the Ti–Al bilayer 10 + 30 nm thick, through the measurement of the resistance as a function of the temperature

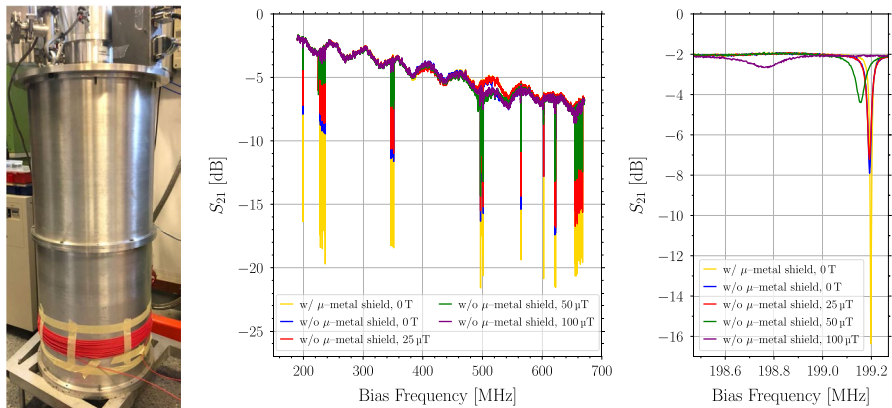


**Fig. 6** *Left panel:* Picture of the testbed cryostat with a coil generating a tunable static magnetic field on the focal plane. *Central panel:* Amplitude of the  $S_{21}$  parameter measured, for the 31-pixel prototype, in dark conditions and at an operating temperature of 150 mK, under different magnetic fields. *Right panel:* Zoom on the first resonance of the *central panel*

order to trap the magnetic field inside them. The *central* and the *right panel* of Fig. 6 show the amplitude of the  $S_{21}$  measured, for the prototype, in dark conditions and at an operating temperature of 150 mK, and a zoom of the first resonance. As we can see, the effect is not negligible and we even needed to attenuate the geomagnetic



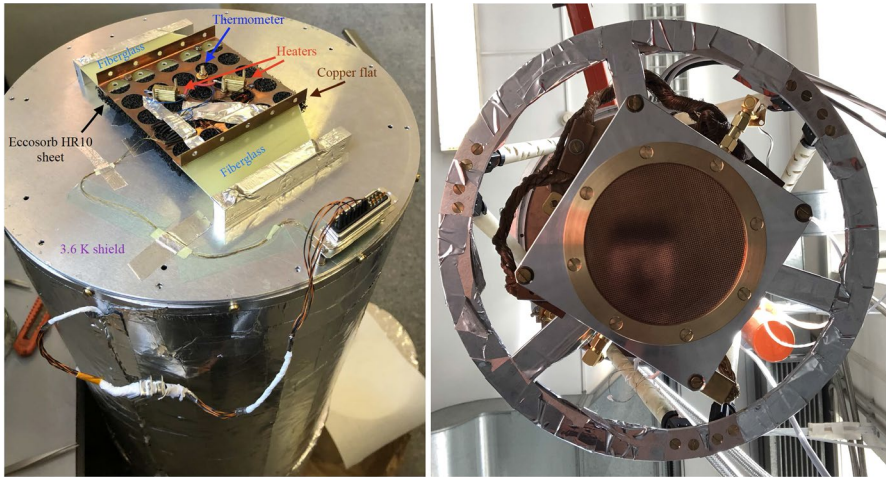


**Fig. 7** *Left panel:* Picture of the temperature-controlled black-body calibrator. *Right panel:* Picture of the detector holder closed with the 90 GHz-centered band-pass filter and mounted in the testbed cryostat

field by means of a  $\mu$ -metal shield placed outside the cryostat. For these reasons, we included a Cryoperm 10  $\mu$ -metal shield at 4 K in the MISTRAL cryostat, as shown in Fig. 1.

The optical characterisation has been performed at the MISTRAL operating temperature, 270 mK, and by means of a temperature-controlled black-body calibrator with a base temperature of 3.6 K, shown in the *left panel* of Fig. 7, [30]. The calibrator consists of an ECCOSORB HR10 sheet, glued on a thick lightened copper flat which is thermally insulated by two fiberglass sheets. Two resistors are used to heat the copper flat, the temperature of which is sensed by a thermometer. The black-body radiation illuminates the detector array after passing through a 240 GHz low-pass filter at 1 K and a 90 GHz-centered band-pass filter, with  $\sim 20$  GHz bandwidth, which closes the detector holder, as shown in the *right panel* of Fig. 7.

The black-body calibrator has been set in order to generate an approximate triangular modulation with a period of 200 s and a peak-to-peak amplitude  $\Delta T_{BB} = 0.48$  K ( $= 4.53$  K  $- 4.05$  K), which corresponds to an in-band power signal  $\Delta P_{BB} = 0.39$  pW ( $= 3.73$  pW  $- 3.34$  pW). This modulated signal, measured by the detectors, is shown in the *left panel* of Fig. 8. Comparing the peak-to-peak amplitude measured by the detectors with  $\Delta P_{BB}$ , we can obtain the responsivity. Then, measuring the noise power spectrum, under a stable 3.6 K radiative background, we estimated the noise equivalent power (NEP), as shown in the *right panel* of Fig. 8. In this plot, we also report the frequency range of interest for MISTRAL, namely the ones corresponding to the scanning speed of the observation strategy ( $v \sim 25$  arcsec/s), the value of the photon NEP of the 3.6 K black-body,  $NEP_{\gamma, 3.6K} = 2.5 \times 10^{-17}$  W/ $\sqrt{\text{Hz}}$  and the photon NEP expected at SRT due to the Earth's atmosphere,  $NEP_{\gamma, atm} = 9 \times 10^{-17}$  W/ $\sqrt{\text{Hz}}$ . For our estimates, we

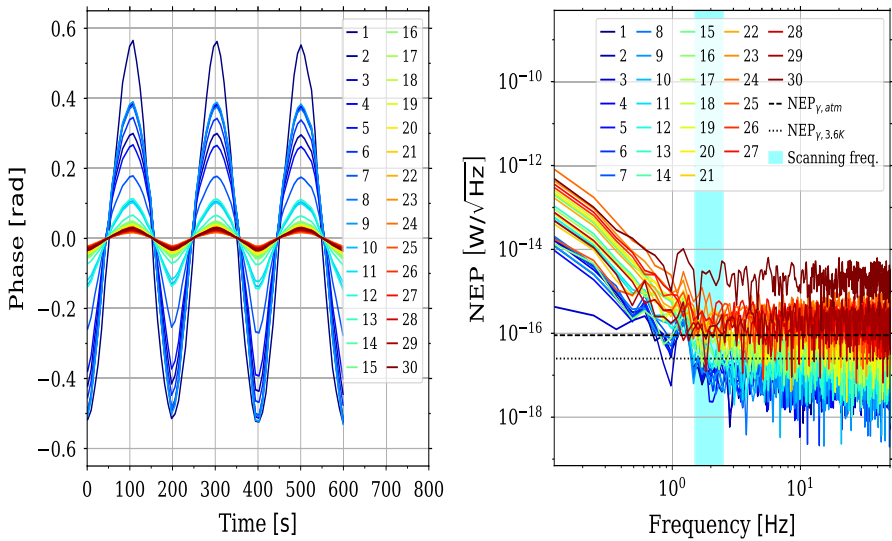


**Fig. 8** *Left panel:* Phase time-streams of the detectors under the modulation of the temperature of the black-body source. Different colours are for different pixels. *Right panel:* Noise equivalent power for all the detectors (different colours are for different pixels). The *dotted* and *dashed* lines represent  $NEP_{\gamma,3.6K}$  and  $NEP_{\gamma,atm}$ , respectively. The *cyan area* indicates the frequency range of interest of MISTRAL, defined by the scanning speed of the observation strategy

assumed that the optical coupling efficiency of each detector to the source is the same and equal to 1, therefore they are to be considered as lower limits for the responsivity and as upper limits for the NEP.

Comparing the measured NEP (that in first approximation is the square root of the quadrature sum between the intrinsic detector NEP and the photon NEP of the source used to measure it, namely the 3.6 K black-body,  $NEP_{\gamma,3.6K}$ ), in the frequency range of interest for MISTRAL, we can say that a third of the detectors shows photon-noise limited performance. Assuming the linearity of the detectors, we could say that two thirds of the detectors show photon-noise limited performance for the background expected for MISTRAL, but this has to be demonstrated through dedicated measurements with a black-body producing a power load as similar as possible to the one expected at the Gregorian focus of SRT, 14 pW considering mainly the contribution due to the Earth's atmosphere, or better in the MISTRAL experimental setup.

As a final consideration, we highlight that, at the operating temperature of 270 mK and under the  $\sim 3$  pW background, we did not measure any substantial changes in the detector  $Q_i$  with respect to the dark condition. This is in agreement with the BCS theory that, for our KID design, predicts a reduction of  $Q_i$  by a factor 1.002. Similarly, under the 14 pW background (the nominal sky load expected at SRT), the reduction of  $Q_i$  is expected to be a factor 1.073 with respect to the  $\sim 3$  pW background condition. This means that the performance under the



14 pW load is expected to be comparable with the one shown in this paper for the  $\sim 3$  pW load.

## 4 Conclusions

MISTRAL will enhance the Sardinia Radio Telescope allowing high angular resolution observations in the W-band. It will provide a wide field (4 arcmin diameter, approximately Nyquist sampled at the diffraction limit of 13 arcsec FWHM) continuum receiver for the W-band, complementing the multi-beam coherent spectroscopic receiver for the same band which will be installed at the Sardinia Radio Telescope [31]. This camera will be available as a facility instrument for the radio-astronomy community and with an expected atmospheric-limited overall sensitivity lower than 6 mJy in 1 s of integration MISTRAL will allow continuum surveys of the mm-wave sky with a variety of scientific targets.

**Acknowledgements** The Enhancement of the Sardinia Radio Telescope (SRT) for the study of the Universe at high radio frequencies is financially supported by the National Operative Program (Programma Operativo Nazionale-PON) of the Italian Ministry of University and Research Research and Innovation 2014-2020, Notice D.D. 424 of 28-02-2018 for the granting of funding aimed at strengthening research infrastructures, in implementation of the Action II.1-Project Proposal PIR01\_00010.

**Funding** Open access funding provided by Università degli Studi di Roma La Sapienza within the CRUI-CARE Agreement.

**Open Access** This article is licensed under a Creative Commons Attribution 4.0 International License, which permits use, sharing, adaptation, distribution and reproduction in any medium or format, as long as you give appropriate credit to the original author(s) and the source, provide a link to the Creative Commons licence, and indicate if changes were made. The images or other third party material in this article are included in the article's Creative Commons licence, unless indicated otherwise in a credit line to the material. If material is not included in the article's Creative Commons licence and your intended use is not permitted by statutory regulation or exceeds the permitted use, you will need to obtain permission directly from the copyright holder. To view a copy of this licence, visit <http://creativecommons.org/licenses/by/4.0/>.

## References

1. R.A. Sunyaev, Y.B. Zeldovich, *Astrophys. Space Sci.* **7**, 3–19 (1970). <https://doi.org/10.1007/BF00653471>
2. A.D. Hincks et al. (2021). <https://arxiv.org/abs/2107.04611>
3. R. Adam et al., *Astron. Astrophys.* **586**, A122 (2016). <https://doi.org/10.1051/0004-6361/201527616>
4. R. Adam et al., *Astron. Astrophys.* **614**, A118 (2018). <https://doi.org/10.1051/0004-6361/201731950>
5. <http://www.terahertz.co.uk/qmc-instruments-ltd>
6. <https://rogerscorp.com/advanced-electronics-solutions/ro3000-series-laminates/ro3003-laminates>
7. <https://www.chasecryogenics.com/products>
8. E.S. Battistelli et al. (2021). <https://doi.org/10.48550/ARXIV.2204.04222>
9. G. D'Alessandro et al., *EPJ Web of Conferences* **257**, 00012 (2022). <https://doi.org/10.1051/epjconf/202225700012>
10. A. Coppolecchia et al., *J. Low Temp. Phys.*, This Special Issue (2021)
11. <http://www.srt.inaf.it/>

12. P. Bolli et al., *J. Astron. Instrum.* **04**(03n04), 1550008 (2015). <https://doi.org/10.1142/S2251171715500087>
13. <https://greenbankobservatory.org/science/telescopes/gbt/>
14. S. Dicker et al., *J. Low Temp. Phys.* **176**, 808–814 (2014). <https://doi.org/10.1007/s10909-013-1070-8>
15. P.K. Day et al., *Nature* **425**, 817 (2003). <https://doi.org/10.1038/nature02037>
16. S. Doyle et al., *J. Low Temp. Phys.* **151**, 530 (2008). <https://doi.org/10.1007/s10909-007-9685-2>
17. A. Paiella et al., in *2017 16th International Superconductive Electronics Conference (ISEC)*, vol. 1 (2017). <https://doi.org/10.1109/ISEC.2017.8314223>
18. A. Paiella et al., *J. Cosmol. Astropart. Phys.* **01**, 039 (2019). <https://doi.org/10.1088/1475-7516/2019/01/039>
19. S. Masi et al., *J. Cosmol. Astropart. Phys.* **07**, 003 (2019). <https://doi.org/10.1088/1475-7516/2019/07/003>
20. A. Coppolecchia et al., *J. Low Temp. Phys.* **199**, 130–137 (2020). <https://doi.org/10.1007/s10909-019-02275-7>
21. A. Paiella et al., *J. Low Temp. Phys.* **184**, 97 (2016). <https://doi.org/10.1007/s10909-015-1470-z>
22. A. Catalano et al., *Astron. Astrophys.* **580**, A15 (2015). <https://doi.org/10.1051/0004-6361/201526206>
23. A. Catalano et al., *Astron. Astrophys.* **641**, A179 (2020). <https://doi.org/10.1051/0004-6361/202038199>
24. B. Aja et al., in *IEEE/MTT-S International Microwave Symposium (IMS)* (2020), pp. 932–935. <https://doi.org/10.1109/IMS30576.2020.9223828>
25. <https://www.ansys.com/it-it/products/electronics/ansys-hfss>
26. S. Shu et al., *IEEE Trans. Terahertz Sci. Technol.* **86**, 605–612 (2018). <https://doi.org/10.1109/TTHZ.2018.2873127>
27. M. Roesch et al., (2011) <https://doi.org/10.48550/ARXIV.1212.4585>
28. S. Gordon et al., *J. Astr. Instr.* **05**, 1641003 (2016). <https://doi.org/10.1142/S2251171716410038>
29. A. Paiella et al., *J. Phys. Conf. Ser.* **1182**, 012005 (2019). <https://doi.org/10.1088/1742-6596/1182/1/012005>
30. A. Paiella et al., *J. Cosmol. Astropart. Phys.* **06**, 009 (2022). <https://doi.org/10.1088/1475-7516/2022/06/009>
31. A. Navarrini et al., in *Proceedings of the 31st Symposium on Space Terahertz Technology, ISSTT*, vol. 2020 (2020), pp. 139–141

**Publisher's Note** Springer Nature remains neutral with regard to jurisdictional claims in published maps and institutional affiliations.